NANO MICRO small

# Supporting Information

for *Small*, DOI: 10.1002/smll.201800659

# Nonhierarchical Heterostructured $Fe_2O_3/Mn_2O_3$ Porous Hollow Spheres for Enhanced Lithium Storage

*Wenhao Ren, Dongna Liu, Congli Sun, Xuhui Yao, Jian Tan, Chongmin Wang,* Kangning Zhao, Xuanpeng Wang, Qi Li,* and Liqiang Mai**

# Supporting Information

## Non-Hierarchical Heterostructured $Fe_2O_3/Mn_2O_3$ Porous Hollow Spheres for Enhanced Lithium Storage

*Wenhao Ren, Dongna Liu, Congli Sun, Xuhui Yao, Jian Tan, Chongmin Wang,* Kangning Zhao, Xuanpeng Wang, Qi Li* and Liqiang Mai**

Dr. Wenhao Ren, Ms. Dongna Liu, Mr. Xuhui Yao, Mr. Jian Tan, Mr. Kangning Zhao, Mr. Xuanpeng Wang, Prof. Qi Li, Prof. Liqiang Mai
State Key Laboratory of Advanced Technology for Materials Synthesis and Processing, Wuhan University of Technology, Wuhan 430070, China
Dr. Wenhao Ren
School of Chemistry, Faculty of Science, The University of New South Wales, Sydney, New South Wales 2052, Australia
Dr. Congli Sun, Prof. Chongmin Wang
Environmental Molecular Sciences Laboratory Pacific Northwest National Laboratory Richland, WA 99352 (USA)

E-mail: qi.li@whut.edu.cn; mlq518@whut.edu.cn

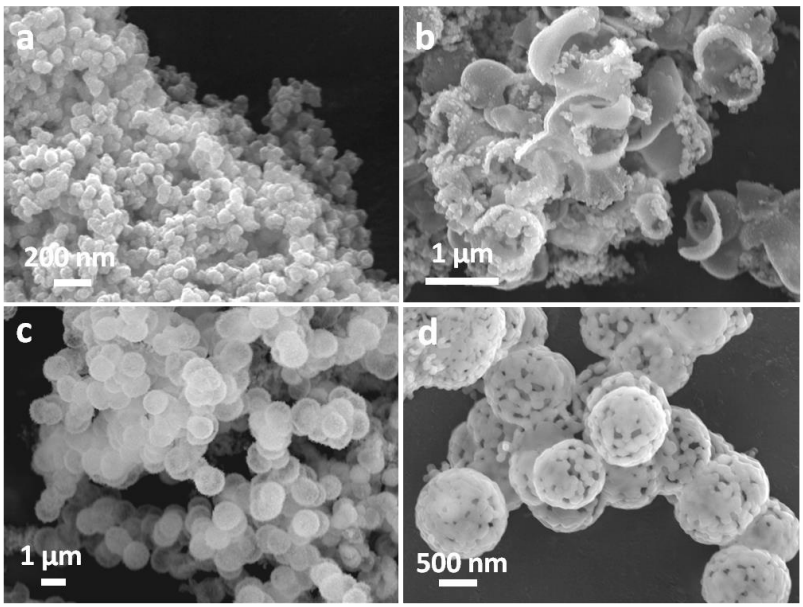


**Figure S1.** Typical SEM images of the sample after the solvothermal reaction of (a) 0.5 h, (b) 1 h, (c) 24 h, and (d) after calcination.

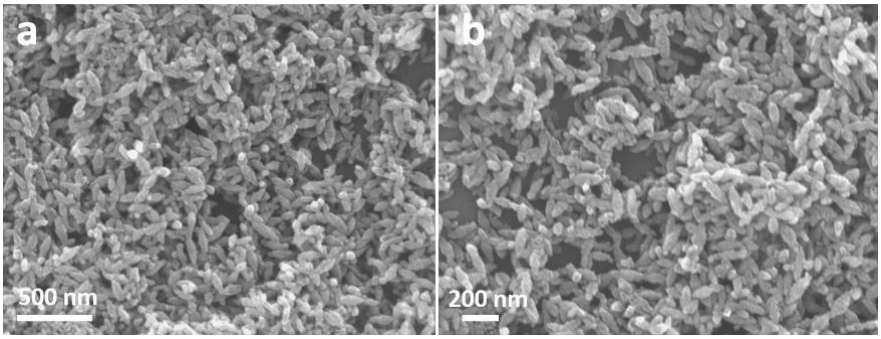


**Figure S2**. SEM images of the sample synthesized without oxalic acid.

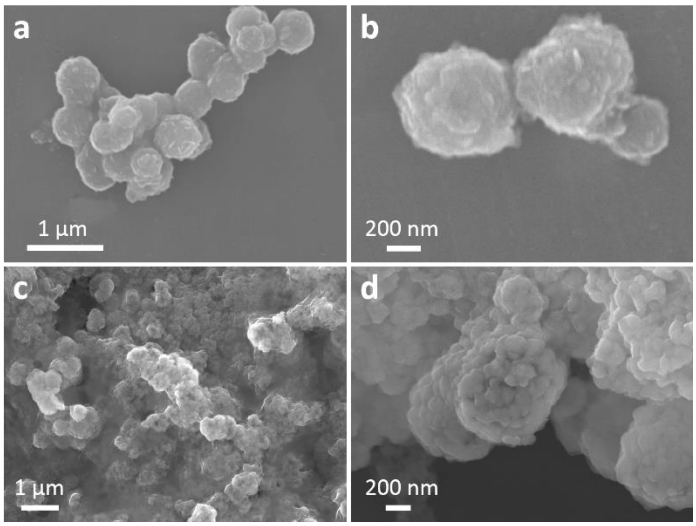


**Figure S3**. a,b) SEM images of the sample synthesized with a $Fe^{3+}$ to $Mn^{2+}$ molar ratio of 3:7. c,d) SEM images of the sample synthesized with a $Fe^{3+}$ to $Mn^{2+}$ molar ratio of 7:3.

The formation mechanism of porous hollow spheres is identified as a co-bonding induced self-assembly process based on the small lattice mismatches (< 1%) between $(104)_{Fe2O3}$ and $(222)_{Mn2O3}$. The ratio of $Fe^{3+}$ to $Mn^{2+}$ is crucial for the formation of uniform morphology. As shown in Figure S3, the porous characteristic disappears in the sample with a lower $Fe^{3+}$ to $Mn^{2+}$ ratio of 3: 7, meanwhile more discrete nanoparticles are obtained in the sample with a higher $Fe^{3+}$ to $Mn^{2+}$ ratio of 7: 3.

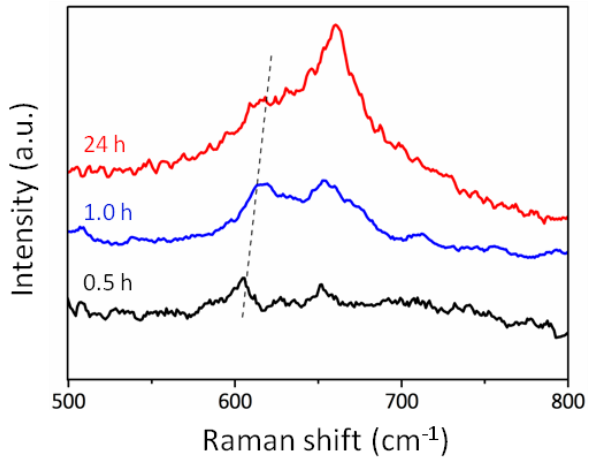


**Figure S4.** Raman spectra after the reaction time of 0.5 h ($FeO_x$), 1 h ($Fe_{1.44}Mn_{0.56}O_x$), and 24 h ($Fe_{1.17}Mn_{0.83}O_x$) from 500 $cm^{-1}$ to 800 $cm^{-1}$.

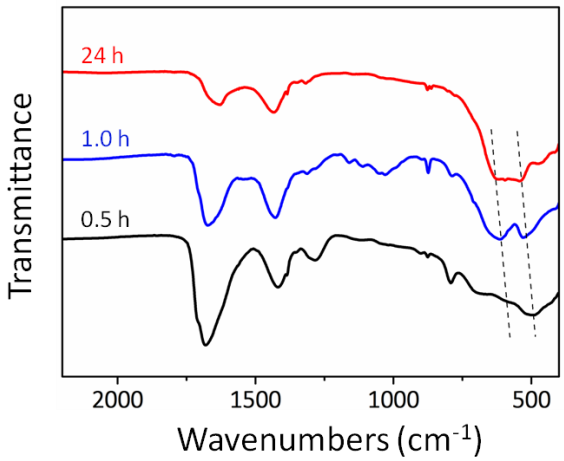


**Figure S5.** FTIR spectra after the reaction time of 0.5 h ($FeO_x$), 1 h ($Fe_{1.44}Mn_{0.56}O_x$), and 24 h ($Fe_{1.17}Mn_{0.83}O_x$).

The FTIR peaks at 500 $cm^{-1}$ and 570 $cm^{-1}$ can be assigned to the Fe-O/Mn-O, and it exhibits similar peaks shift towards higher wavenumber region as the reaction time increases, which is consistent with the Raman results.

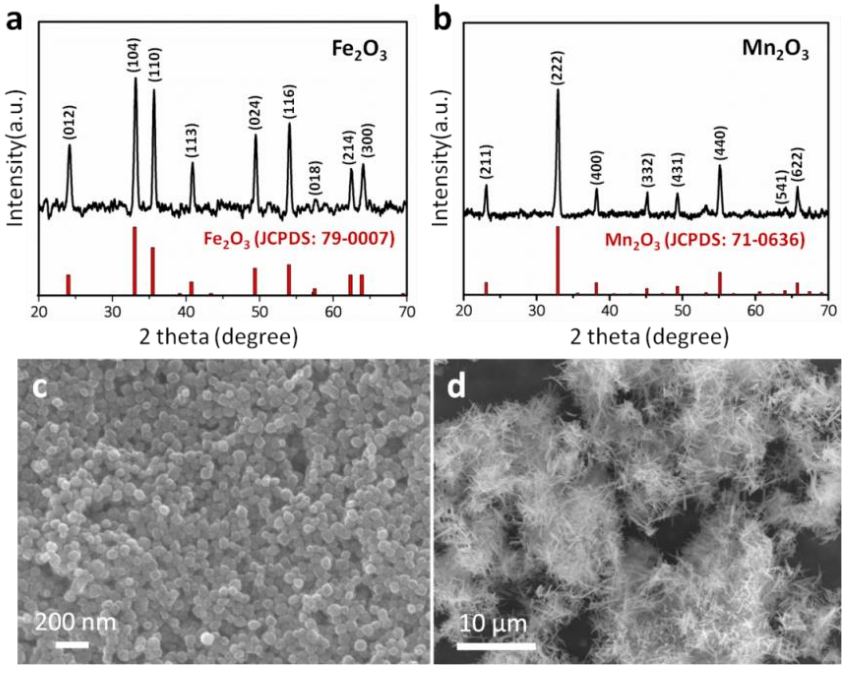


**Figure S6.** a,b) XRD patterns of $\alpha$-$Fe_2O_3$ and $\alpha$-$Mn_2O_3$. c,d) SEM images of $\alpha$-$Fe_2O_3$ and $\alpha$-$Mn_2O_3$.

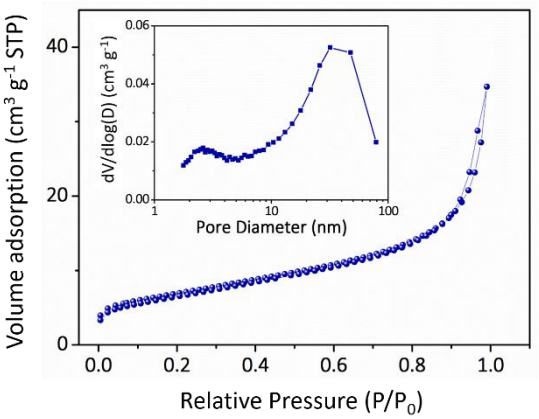


**Figure S7.** Nitrogen adsorption-desorption isotherm and corresponding pore size distribution (inset) of $Fe_2O_3/Mn_2O_3$.

The low specific surface area of NHPHS $Fe_2O_3/Mn_2O_3$ (24.2 $m^2$ $g^{-1}$) can be attributed to two aspects. On the one hand, the heat treatment procedure leads to the crystal growth of building block nanoparticles, and thus decrease the surface area. On the other hand, the relatively high atomic weight of $Fe_2O_3/Mn_2O_3$ results in the low gravimetric surface area.

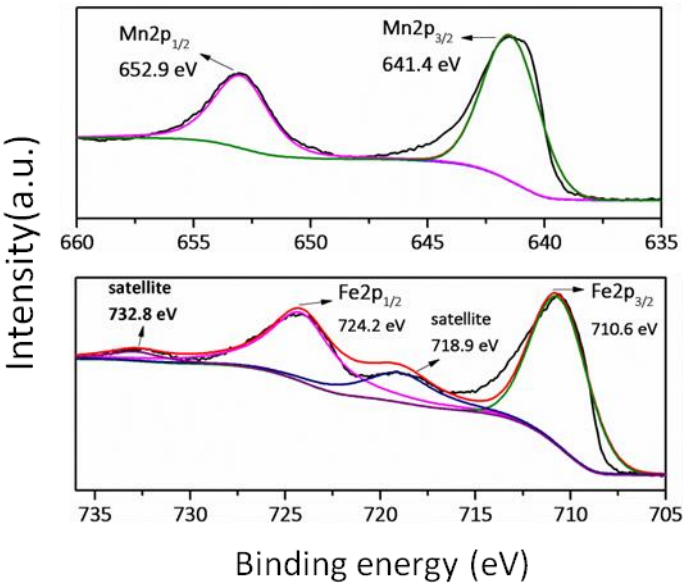


**Figure S8.** XPS of Mn 2p and Fe 2p spectra of $Fe_2O_3/Mn_2O_3$.

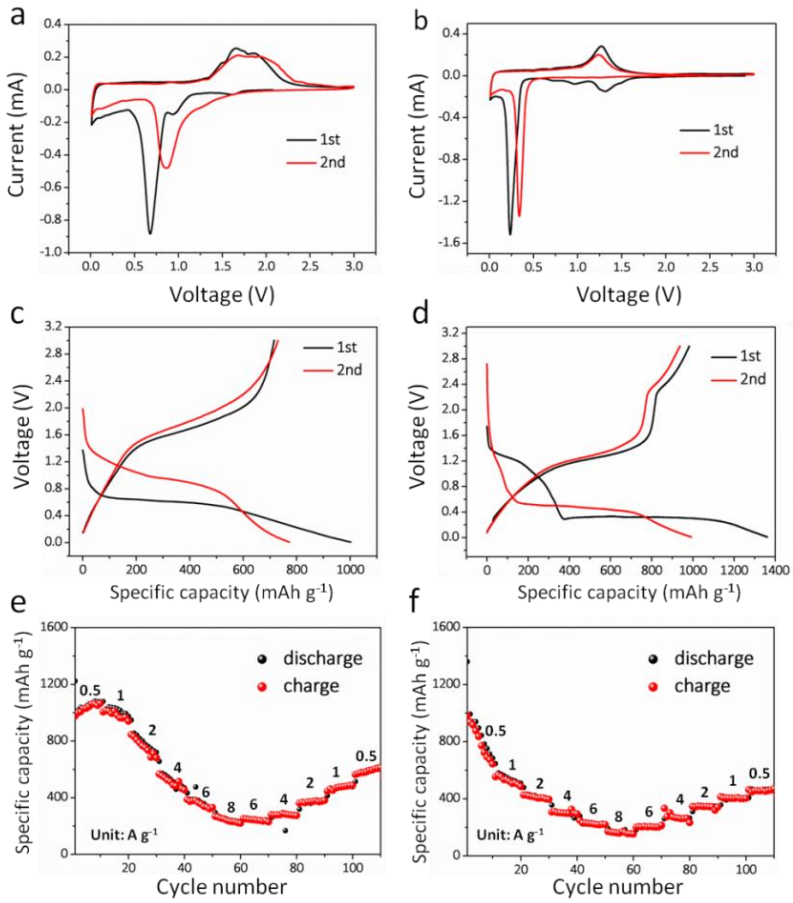


**Figure S9.** a,b) CV profiles of $Fe_2O_3$ and $Mn_2O_3$ at a scan rate of 0.1 mV $s^{-1}$. c,d) Charge-discharge curves of $Fe_2O_3$ and $Mn_2O_3$ at 1A $g^{-1}$. e,f) Rate performance of $Fe_2O_3$ and $Mn_2O_3$ at different current densities of 0.5, 1, 2, 4, 6, 8 A $g^{-1}$.

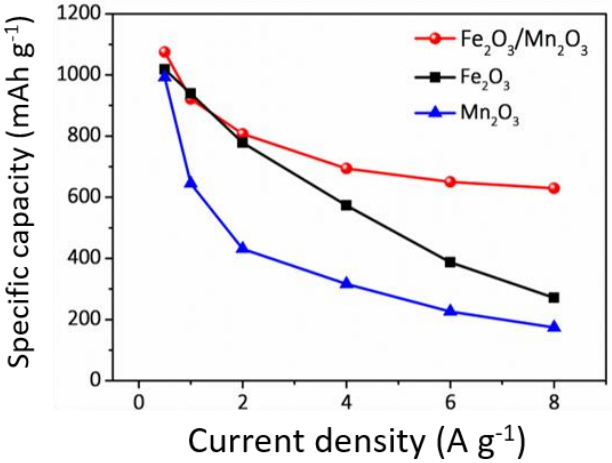


**Figure S10.** Discharge capacity *vs*. current density of $Fe_2O_3/Mn_2O_3$, $Fe_2O_3$ and $Mn_2O_3$.

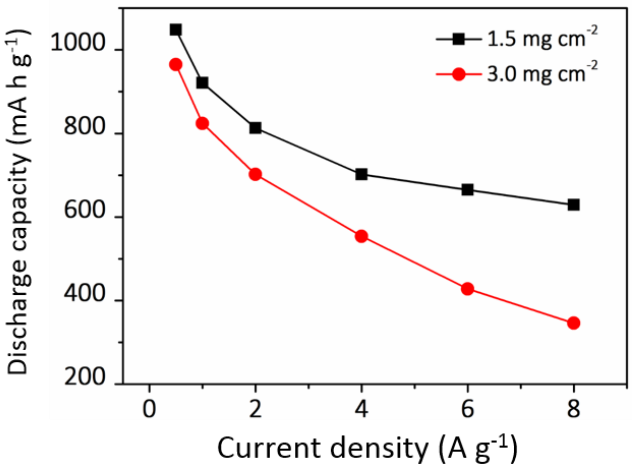


**Figure S11.** Discharge capacities of NHPHS $Fe_2O_3/Mn_2O_3$ at different mass loading of 1.5 and 3.0 mg $cm^{-2}$ from 0.5 to 8 A $g^{-1}$.

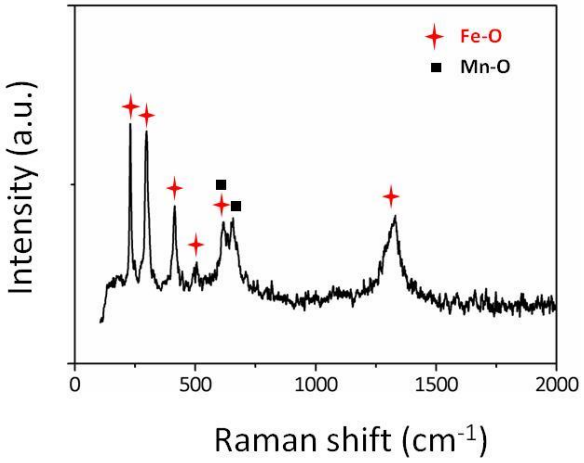


**Figure S12.** Raman spectrum of $Fe_2O_3/Mn_2O_3$.

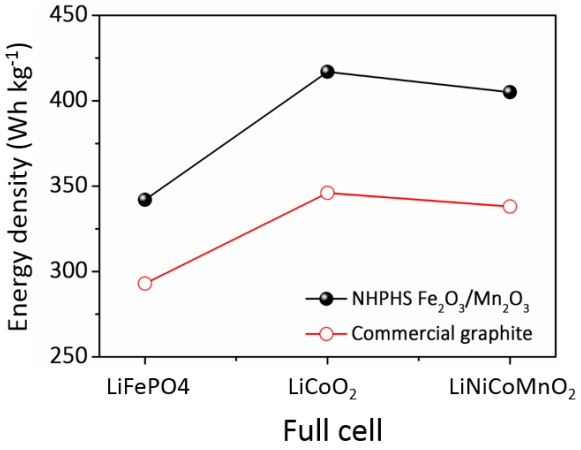


**Figure S13.** The theoretical energy density of various full batteries based on $LiFePO_4$, $LiCoO_2$, and $LiNiCoMnO_2$ cathodes, and NHPHS $Fe_2O_3/Mn_2O_3$ and commercial graphite anodes.

The theoretical energy density of various full batteries including $LiCoO_2$//$Fe_2O_3/Mn_2O_3$, $LiFePO_4$//$Fe_2O_3/Mn_2O_3$, and $LiNiCoMnO_2$//$Fe_2O_3/Mn_2O_3$ can be calculated to be 239, 291 and 284 Wh $kg^{-1}$, respectively, which shows significant improvement in compassion with commercial graphite anode (340 mA h $g^{-1}$).

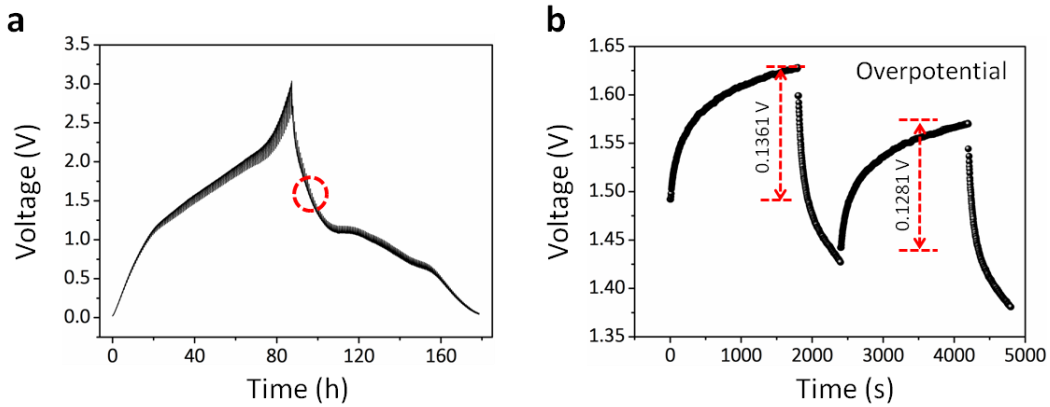


**Figure S14.** a) The potential response of GITT measurement. b) The magnified image of the region in a).

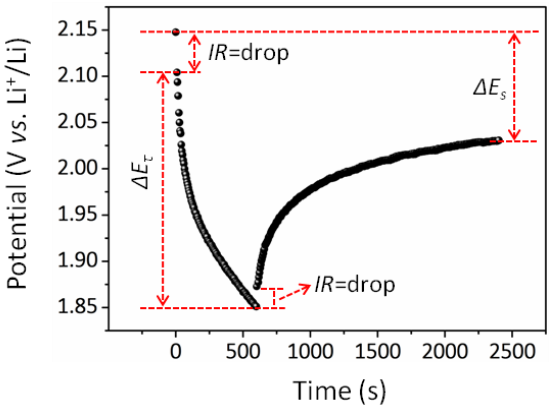


**Figure S15.** The GITT potential response curve with time.

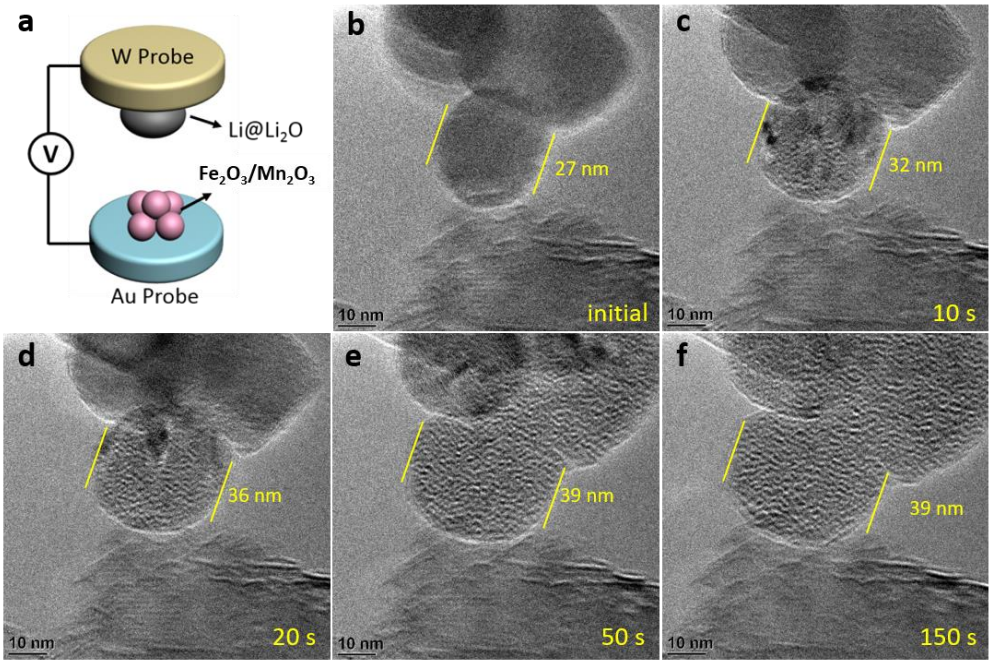


**Figure S16.** a) Schematic of in situ TEM device. b-f) The high-resolution in situ TEM test of targeted building blocks of $Fe_2O_3/Mn_2O_3$ during lithiation.

**Table S1.** Time-dependent ICP results of the samples.

| Reaction time | Element | Concentration ($\mu g\ g^{-1}$) | Atomic ratio (Fe : Mn) |
|---|---|---|---|
| 0.5 h | Fe | 452498 | 957:1 |
| | Mn | 473 | |
| 1 h | Fe | 33392 | 2.6:1 |
| | Mn | 12844 | |
| 24 h | Fe | 278680 | 1.4:1 |
| | Mn | 196250 | |
| 24 h (After calcination) | Fe | 264320 | 1.4:1 |
| | Mn | 184358 | |

**Table S2.** Electrochemical properties of iron or manganese based anodes for LIBs.

| **Products** | **Cycle number (capacity retention)** | **Discharge capacity (current density)** | **Initial Colombic Efficiency** | **Reference** |
|---|---|---|---|---|
| Our work | 600 (89.3%) | 638 mA h $g^{-1}$ (8 A $g^{-1}$) | 70% | / |
| $\beta$-$MnO_2$/$\alpha$-$Fe_2O_3$ | 200 (83.3%) | 881 mA h $g^{-1}$ (4 A $g^{-1}$) | 69% | S1 |
| Porous $\alpha$-$Fe_2O_3$ nanosheets | 400 (70.2%) | 433 mA h $g^{-1}$ (20 A $g^{-1}$) | 70% | S2 |
| $Fe_2O_3$-carbon nanofibers | 300 (84%) | 491 mA h $g^{-1}$ (5 A $g^{-1}$) | 68% | S3 |
| 1D $\alpha$-$Fe_2O_3$ | 1200 (77.6%) | 783 mA h $g^{-1}$ (5 A $g^{-1}$) | 80% | S4 |
| 1D $MnO_x$/C | 200 (98.3%) | 91 mA h $g^{-1}$ (2 A $g^{-1}$) | 59% | S5 |
| Polyhedron $Mn_2O_3$ | 1200 (98.6%) | 686.7 (2 A $g^{-1}$) | 60% | S6 |
| Monodisperse $\alpha$-$Mn_2O_3$ | 100 (95.1%) | 435 (3.2 A $g^{-1}$) | 67% | S7 |
| Graphene/$Mn_3O_4$ | 100 (87.5%) | 308 (3.2 A $g^{-1}$) | 66% | S8 |

**Reference**


[S1] X. Gu, L. Chen, Z. Ju, H. Xu, J. Yang, Y. Qian, *Adv. Funct. Mater.* **2013**, *23*, 4049-4056.

[S2] K. Cao, L. Jiao, H. Liu, Y. Liu, Y. Wang, Z. Guo, H. Yuan, *Adv. Energy Mater.* **2015**, *5*, 1401421.

[S3] J. S. Cho, Y. J. Hong, Y. C. Kang, *ACS Nano* **2015**, *9*, 4026-4035.

[S4] K. Zhao, M. Wen, Y. Dong, L. Zhang, M. Yan, W. Xu, C. Niu, L. Zhou, Q. Wei, W. Ren, X. Wang, L. Mai, *Adv. Energy Mater.* **2017**, *7*, 1601582.

[S5] Z. Cai, L. Xu, M. Yan, C. Han, L. He, K. M. Hercule, C. Niu, Z. Yuan, W. Xu, L. Qu, K. Zhao, L. Mai, *Nano Lett.* **2015**, *15*, 738-744.

[S6] K. Cao, L. Jiao, H. Xu, H. Liu, H. Kang, Y. Zhao, Y. Liu, Y. Wang, H. Yuan, *Adv. Sci.* **2016**, *3*, 1500185.

[S7] J. Henzie, V. Etacheri, M. Jahan, H. Rong, C. N. Hong, V. G. Pol, *J. Mater. Chem. A* **2017**, *5*, 6079-6089.

[S8] J. G. Wang, D. Jin, R. Zhou, X. Li, X. R. Liu, C. Shen, K. Xie, B. Li, F. Kang, B. Wei, *ACS Nano* **2016**, *10*, 6227-6234.